# A gallic acid based metal organic framework derived NiS/C anode for sodium ion batteries

Mehbare Dogrusoz, Thomas Devic, Ali Şems Ahsen, Rezan Demir-Cakan

# A Gallic Acid Based Metal Organic Framework Derived NiS/C Anode for Sodium Ion Batteries

*Mehbare Dogrusoz[a,b], Thomas Devic [c], Ali Şems Ahsen[d], Rezan Demir-Cakan[*,a,b]*

*a. Gebze Technical University, Department of Chemical Engineering, 41400 Gebze, Kocaeli, Turkey*

*b. Gebze Technical University, Institute of Nanotechnology, 41400 Gebze, Kocaeli, Turkey*

*c. Institut des Materiaux Jean Rouxel (IMN),´ UMR 6502, CNRS Universitéde Nantes, 44322 Nantes, France*

*d. Gebze Technical University, Department of Physics, 41400 Gebze, Kocaeli, Turkey*

** Corresponding Authors. E-mails: demir-cakan@gtu.edu.tr*

**Abstract**

Strategies are tailed to enhance the electro-active material capacity and cycle life of the sodium-ion batteries. Amongst electrode materials, metal-organic framework derived anode materials starts to stand out because of their versatile compositions, structures and textures, leading to high specific surface area and more active electrochemical reaction sites. Herein, firstly a Ni-MOF is prepared from a bio-available organic linker, namely gallic acid, in a begin solvent (water). Then a nickel sulfide/carbon (NiS/C) composite is synthesized by concurrent sulfuration and carbonization under nitrogen flow at 600 °C. Carbon encapsulated NiS particles are formed in which carbon framework not only prevents the volume expansion of NiS during discharge but also gives rise to higher conductivity. Resulting NiS/C composite is tested as a potential anode material for sodium-ion batteries and delivered around 210 mAh·g-1 capacity at 591 mA·g-1 current density after 500 charge/discharge cycles. Even at higher current densities (at 2950 mA·g-1), the discharge capacity reached 250 mAh·g-1. Na+ ion diffusion rate is calculated through Warburg Impedance analysis where 1.87·10-16 and 3.5·10-15 S·cm-1 are obtained initially and after the cell is terminated, respectively.

## 1. Introduction

Sodium ion batteries have large potential to replace the lithium ion batteries due to the similar physical/chemical properties, lower cost, geographically uniform distribution in parallel sustainability and more environment friendly nature [1-3]. Thus to catch the closest performance to lithium ion batteries, the works on sodium ion battery have been accelerated since 2010 [4]. On the other hand, lower ionization potential of the sodium ion causes lower operating voltage and consequently lower energy density. Moreover, the larger ionic radius of the sodium ion cause a sluggish diffusion through the host material [2]. Therefore, search for the alternative electrode materials for commercialization is mainly dependent on obtaining stable capacity and long cycling capability at high current density.

Regarding the anode materials in the field of sodium ion batteries, the use of hard carbons are the milestone after the experimental conformity of the Steven and Dahn's study in 2000 [5]. However, poor cycling and rate capability as well as relatively low capacity of hard carbons hinder their practical application [6]. Therefore, other possible anodes such as metal sulfides, selenides, oxides, phosphides, tellurides including single, binary metals have been proposed [7-10]. Among them, metal sulfides are one of the promising anode candidates owing to the rich redox behaviour, high $Na^+$ storage capacity and low cost [11]. $Na_2S$ is the discharge product of metal sulfides (together with metallic Ni) that has higher conductivity than that of $Na_2O$. Besides to that, metal-sulfur bonds are weaker than metal-oxygen bond, whereby this properties can provide advantages for the conversion reaction kinetics compared to the metal oxide counterparts [11, 12]. Nickel sulfides have large family members (i.e. NiS, $NiS_2$, $Ni_3S_4$, $Ni_3S_2$, $Ni_7S_6$, $Ni_9S_8$ etc.) with theoretical capacity values that are much higher than hard carbons (i.e. NiS: 591 $mAh{\cdot}g^{-1}$, $NiS_2$: 879 $mAh{\cdot}g^{-1}$, $Ni_2S_3$: 446 $mAh{\cdot}g^{-1}$) [13-16]. On the other hand, cycling performance of nickel sulfides is poor due to the volume changes during the $Na^+$ insertion/extraction as well as irreversible capacity loss caused by the polysulfide dissolution within the electrolyte which is well known phenomena from Li-S batteries [17]. To surpass these challenges, the most common methods are the use of $Ni_xS_y$ embedded into porous carbon matrix as well as reduction of the active material size in order to shorten the ionic diffusion pathway [18]. To do so, $NiS_x$/CNT composite was prepared via solvothermal solution route followed by thermal treatment. As a sodium ion battery anode, $NiS_x$/CNT composite delivered up to 400 $mAh{\cdot}g^{-1}$ stable capacity during 200 cycles at 100 $mA{\cdot}g^{-1}$ current density [19]. In another study, NiS synthesized by refluxing method reached a capacity of approximately 500 $mAh{\cdot}g^{-1}$ at 100 $mAh{\cdot}g^{-1}$ current density after the $50^{th}$ cycles [20].

As an alternative method, Metal Organic Frameworks (MOFs) were also used to prepare porous carbon electrodes. These solids are built of metal ions connected together through organic linkers and could present very high surface area and pore volume which are of interest e.g. for gas capture and storage [21, 22]. In the field of electrochemical energy storage, they are used either as prepared, but also as sacrificial materials to prepare by proper calcination nanostructured oxides or carbons [23]. The first application of the MOFs as a carbon anode template date backed in 2008, where MOF-5 (a zinc terephthalate framework) was thermally treated under inert atmosphere above the decomposition temperature of the linker [24]. Latter while linker turned into carbonaceous framework, metal ions are either transformed to metal oxide or reduced to metal (0) depending on the nature of the linker and applied temperature. This strategy was then applied in the presence of sulfur, selenium or phosphorous to produce respectively $M_xS_y$, $M_xSe_y$ or $M_xP_y$ phases [25, 26].

Herein, we focused on a small pore Ni-MOF formulated as $Ni(C_7H_4O_5).2H_2O$ [27]. While MOFs are generally prepared from synthetic ligands in harmful organic solvents (e.g. dimethylformamide), this MOF is readily prepared in water from a naturally occurring, non-toxic phenolic molecule, namely gallic

acid. This solid has already been utilized as a sacrificial material to prepare carbons doped with metallic nanoparticles [28]. However, to the best of our knowledge not used to prepare NiS/C composite. In order to obtain the desired NiS/C anode composite at one-step process, MOF powder was mixed with the sublimed sulfur and the mixture was heated at 600 °C under pure nitrogen atmosphere leading to the carbonization of the linker and sulfuration of Ni ion. The resulting composite was evaluated as an anode material for Na ion batteries.

## 2. Experimental

### 2.1 Material Preparation

$Ni(C_7H_4O_5).2H_2O$ was prepared using a room pressure route derived from the one published for the Mg analogue [29]. 0.75 g of gallic acid monohydrate (4 mmol) and 1.02 g of nickel(II) sulfate hexahydrate (3.9 mmol) were placed in a 50 mL round bottom flask in 10 mL of deionized water. 1.6 mL of a 5 M aqueous KOH solution (8 mmol) were added. The mixture was heated under stirring in an oil bath at 80°C for few hours. The resulting solid was recovered by filtration, washed with water and ethanol, and dried in air.

### 2.2 Synthesis of NiS/C Powder

The Ni-MOF and sulfur powders were weighed as 51 mg and 117 mg, respectively. Considering the weight of Ni in MOF, the amount of sulfur was used in excess due to the volatilization above its melting point. The powders were simply blended by agate mortar. Subsequently, the powder was put into a porcelain crucible and transferred to the quartz tube furnace. NiS/C composite was obtained via the sulfuration of Ni-MOF under the pure nitrogen atmosphere by heating up from room temperature to 600 °C with a 2 °C·$min^{-1}$ ramp rate and kept at this temperature for 2 hours. The sample was cooled down naturally at room temperature under continuous nitrogen flowing. Resulting black composite powder was collected from the crucible.

### 2.3 Material Characterization

#### 2.3.1 MOF

X-Ray powder diffraction (XRPD) pattern was collected at room temperature on a Siemens D5000 Diffractometer working in Bragg-Brentano geometry [(θ-2θ) mode] in the range 2θ = 3-40° using Cu Kα radiation. Thermogravimetric analyses (TGA) was performed on a NETZSCH STA 449F5 apparatus under air atmosphere, at a heating rate of 5 °C $min^{-1}$ up to 600°C. Fourier transform infrared spectra were recorded on a Bruker Alpha FT-IR spectrometer equipped with a diamond attenuated total reflectance unit. The spectra were recorded from 4000 to 400 $cm^{-1}$ with a resolution of 2 $cm^{-1}$ at 50 scans.

#### 2.3.2. NiS/C composite

XRPD was performed with Bruker AXS Advance D8 with Cu $K_\alpha$ radiation by 3°$min^{-1}$ scan rate. Powder morphology, elemental mapping, initial electrode surface and post-mortem electrode surface after C-rate test was investigated by using Scanning Electron Microscopy (SEM by FEI/Philips $XL_{30}$ FEG ESEM equipped with Energy Dispersive X-Ray Spectroscopy). NiS/C powder was also analyzed by Scanning Transmission Electron Microscopy (STEM, Hitachi High Tech HT7700). Thermogravimetric Analysis by TA Instruments Q500 were conducted to detect the carbon content of NiS/C composite under air atmosphere with 10 °C·$min^{-1}$ ramp rate up to 700 °C and 850 °C. X-Ray Photoelectron Spectroscopy (XPS) measurements were performed by a SPECS Phoibos 150 Specs charged particle analyzer and SPECS X-Ray source XR 50 operated at 125 W. The analysis chamber for XPS measurements has a base pressure

in the range of $10^{-10}$ mbar. XPS data were obtained in the fixed analyzer transmission mode at 50 eV pass energy and using Al K$\alpha$ X-ray source. The spectrometer was calibrated using Au $4f_{7/2}$ (84.1 eV) photoemission lines and the full width at half-maximum (FWHM) for Au $4f_{7/2}$ was 1.5 eV. The XPS peak deconvolution were performed using a combination of lorentzian and gaussian distributions about 30% and 70% respectively after the subtraction of a Shirley background function [30]. The specific surface area and pore size distribution were detected by Micrometrics 3 Flex 3 port analyser via the Brunauer-Emmett-Teller (BET) and Barrett- Joyner-Halenda (BJH) methods, respectively. HRTEM analysis were conducted with JEOL JEM 2100F to investigate the microstructure of NiS/C powder which is equipped with High Angular Annular Dark Field (HAADF) detector.

**2.3.4 Electrochemical Measurements**

NiS/C powder was mixed with Alginic Acid Sodium (Na-alginate) (Alfa Aeser) binder and C Super P conductive additive with a mass ratio of 80:10:10, respectively, by adding a 1 ml pure water to dissolve the binder. The mixture was stirred overnight to produce a homogenous slurry. Doctor blade was used to coat the slurry onto an aluminium foil, and the resulting electrode was dried in the vacuum oven overnight at 80 °C. The mass loading of the composite was around 1.0 $mg \cdot cm^{-2}$. Electrolyte solution was prepared by dissolving 1M $NaClO_4$ (Alfa Aeser) in Propylene Carbonate (PC, Alfa Aeser) by adding Flouroethylene Carbonate (FEC, Alfa Aeser) with 5% volume ratio. Both coin cell and Swagelok™ test cells were assembled into the Argon filled glove box. Sodium foil was acted as both counter and reference electrodes and glass fiber (Whatman GF/C) was the separator. Galvanostatic charge–discharge tests were conducted with Neware Battery Tester in a voltage range from 0.01V to 3.0 V (vs. $Na/Na^+$). Cyclic Voltammetry test was applied at a scan rate of 0.1 $mV \cdot s^{-1}$ with the same voltage range. Impedance spectra was performed between the 0.1 mHz and 1 MHz with a voltage amplitude of 5 mV with two electrode cell using Biologic VMP-3 galvanostat/potentiostat. The experimental data were fitted by a EC-lab software created ZFit.

## 3. Results and Discussion

$Ni(C_7H_4O_5).2H_2O$ is a 3-D MOF built up from chains of corner sharing $NiO_6$ octahedra connected through each other through hemi-deprotonated gallate ligand to define small triangular channels (**Figure 1a**). This solid was initially prepared under hydrothermal conditions [27], but we here used a room pressure, room bottom flask route, more adapted for the production of larges batches [29]. Powder XRD analysis confirmed the formation of the expected solid (**Figure 1b**), while infrared spectroscopy (**Figure 1c**) indicated the absence remaining free gallic acid (no characteristic band at ca. 1700 $cm^{-1}$). Thermogravimetric analysis further confirmed that this MOF presents a moderate thermal stability (**Figure 1d**), as already reported [27, 29].

**Figure 2a** represents the NiS/C composite X-ray powder diffraction pattern that verifies the nickel sulfide phase formation (JCPDS No: 002-1280). The most apparent peaks were located at 30.1°, 34.5°, 45.7°, 53.5° and 73° referred to the NiS phase [31]. Also the broad and small hump at around the 24° was associated with the existence of amorphous carbon [32]. Additionally, NiS powder was in nanoscale and its crystalline size calculated as 12.6 nm by using Debye Scherer Equation taking into account the full width of the half of the maximum of main XRD peaks at 45.7°. Furthermore, Termogravimetric Analysis (TGA) were performed to calculate the composition contents of the NiS/C composite (**Figure 2b**). Firstly, there is a slight mass increase until 400 °C due to the due to the partial oxidation of NiS/C composite [33]. Later on in the range of 400-530 °C, a sharp mass loss was occurred corresponding to the partial

sulfur decomposition of NiS/C into $NiS_{1-x}$ as well as $CO_2$ formation through combustion of carbon [34-36]. TGA curve between 530-700 °C was ascribed for the conversion of $NiS_{1-x}$ into NiO and $NiSO_4$ confirmed by the intermediate XRD measurement at 700 °C (**Figure SI-1a**). When the temperature was risen up to 850°C, a complete formation of NiS into NiO was evident by the XRD analysis at 850 °C (**Figure SI-1b**). As a whole, based on the TGA measurements carbon content in the NiS/C composite is approximately 28 wt %.

Ultrafine NiS/C particles derived from Ni-Metal Gallate MOF and sulfur was observed by SEM images (**Figure 2c**). Elemental mapping with the overlay, nickel, sulfur and carbon images presented in **Figure 2d-g** depicted that NiS nanoparticles are encapsulated inside carbon particles. Transmission electron microscopy view supported the SEM result that spherical and nanoscale NiS particles (< 20nm) distributed homogeneously and encapsulated within the amorphous carbon (**Figure 2h**). High Resolution TEM analysis showed the lattice fringes clearly with 0.18 nm spacing supporting the good crystallinity of NiS phase (**Figure 2i**). The same d-spacing between lattice fringes was 0.18 nm in which corresponds to (110) planes of NiS particles [31].

The surface valence states and chemical composition of the NiS/C composite were determined by X-ray photoelectron spectroscopy (XPS) measurements at room temperature in ultrahigh vacuum conditions as shown in **Figure 3**. The survey spectrum of NiS/C powder was shown in **Figure 3a**, thereby, the presence of nickel, carbon and sulfur was confirmed as well as oxygen content that might be from the surface contamination and oxygenated functionalities. In **Figure 3b**, the peaks at 871.3eV and 854.0 eV indicated the presence of $Ni2p_{1/2}$ and $Ni2p_{3/2}$ respectively. However, Ni-metal $2p_{1/2}$ and $2p_{3/2}$ peak binding energies were located at 870 eV and 853 eV, respectively. The shift of both peaks to higher binding energy around 1.3 eV supports that nickel was in $Ni^{2+}$ valence state [37, 38]. The reason for the shift of the binding energy to the higher value is the reason of the attraction of sulfur electrons by the nickel atoms. Additionally, sulfur 2p peak was deconvoluted into two main peaks (**Figure 3c**). The peak located at 162.8 eV (blue line) corresponds to the nickel monosulfide formation [39-42]. The investigation of the nickel monosulfide peak showed that the $S2p_{3/2}$ and $S2p_{1/2}$ peaks were located at 162.7 eV and 164.0 eV respectively (while bigger blue dashed line was referring the $S2p_{3/2}$, the smaller one was corresponded to $S2p_{1/2}$). According to the literature, the neutral $S_n^0$ $2p_{3/2}$ binding energy value was in the range from 163.6 eV to 164.2 eV [41]. The energy shift of the $S2p_{3/2}$ peak was around 1.2 eV which was also in accordance with the energy shift of Ni $2p_{3/2}$.

The second peak located at 164.2 eV (light green line) corresponds to the C-S interaction which was deconvoluted in two peaks at 164.1 eV and 165.3 eV relating to $2p_{3/2}$ and $2p_{1/2}$ respectively and showed with dashed light green lines. Therefore the binding energy values indicated that sulfur interacted not only with nickel but also with carbon[40, 43]. In addition, the C-S interaction can also be observed after the deconvolution of C1s peak at 284.6 eV. XPS spectrum of C1s demonstrated four sub-peaks that were located at 284.6 eV, 285.7 eV, 287.4 eV, 289.3 eV and identified as C=C/C-C, C-O/C-S, C=O, COOH/COOR, respectively, (**Figure 3d**) [44, 45].

Brunauer-Emmett-Teller surface area and porosity were also investigated by $N_2$ adsorption-desorption isotherms for the NiS/C composite (**Figure SI-2**). BET surface area was measured as 74 $m^2 \cdot g^{-1}$. The hysteresis was seen between 0.4-0.9 relative pressure value that was indicated to Type IV IUPAC isotherms. Therefore the composite contains in a vast number of mesoporous[46]. The pore size distribution was estimated by using Barrett- Joyner-Halenda (BJH) desorption method and depicted in

**Figure SI-2b**. The peak point of the pore size distribution graph defined the average pore size of 3.62 nm with 0.745 $cm^3 \cdot g^{-1}$ pore volume.

**Figure 4a** depicts the cyclic voltammetry (CV) of the NiS/C anode at a scan rate of 0.1 $mV \cdot s^{-1}$ from 0.01V to 3.0 V (vs $Na/Na^+$) voltage range. The reduction peaks at 1.1 V and 0.4 V corresponds the electrolyte decomposition onto the electrode surface (formation of the SEI) as well as NiS conversion to metallic nickel and $Na_2S$. The reaction between the Na and NiS are carried out as $NiS + 2Na + 2e^- \leftrightarrow Na_2S + Ni$ [47]. Additionally, the small cathodic peak at around 0.012 V indicates the sodiation of amorphous carbon ($xC+Na^++e^- \leftrightarrow NaC_x$). At the anodic scan, there are two peaks at around the 1.6 V and a small hump at 1.3 V that is attributed to NiS reformation from metallic nickel and $Na_2S$. Reverse cathodic scan has a peak located at 0.2 V is expressed as the desodiation of the amorphous carbon [32, 48]. In ongoing cycles, the oxidation and reduction peaks were overlapped with a smaller shift due to the clustering nanoparticles [49]. The galvanostatic charge-discharge profile of the NiS/C is shown in **Figure 4b**. While the initial discharge capacity reached 939 $mAh \cdot g^{-1}$, 632 $mAh \cdot g^{-1}$ charge capacity value was obtained with a 67% initial columbic efficiency. However, for the following cycles, the columbic efficiency reached much higher values and after 100 cycles around 300 $mAh \cdot g^{-1}$ capacity was achieved at 59 $mA \cdot g^{-1}$ current density. Rate performance test was evaluated at various current densities ranging from 59 to 2950 $mA \cdot g^{-1}$ (**Figure 4c)**. The discharge capacities were 500, 450, 400, 300 and 250 $mAh \cdot g^{-1}$ at 59, 295, 591, 1475 and 2950 $mA \cdot g^{-1}$ current densities, respectively. When the current density was turned back to 59 $mA \cdot g^{-1}$, the capacity value reached 450 $mAh \cdot g^{-1}$ at $30^{th}$ cycle, corresponding to a capacity retention of 90% before and after C-rate test (**Figure 4b)**. The electrochemical performance of NiS/C composite performs much better especially at high current density. **Figure 4e** depicts that around 210 $mAh \cdot g^{-1}$ capacity with a good columbic efficiency was obtained after 500 cycles at 591 $mA \cdot g^{-1}$ current density.

The performances of $Ni_xS_y$ electrodes derived from MOFs reported to date were summarized in **Table 1**. First of all, the present study differs from the other reports due to the use of sustainable sources where a naturally occurring phenolic molecule, gallic acid, was used as organic linker to prepare the Ni-MOF structure [50]. For the synthesis protocol, generally multistep approaches were used in which first Ni/C was formed followed by sulfuration contrary to our approach where NiS/C was formed at one-step. Thus, the present approach let to the resulting NiS/C composite with a high NiS content could be an alternative anode material for sodium ion batteries especially at the high current densities. Electrochemical impedance spectroscopy experiments were conducted to elucidate NiS/C anode performance in detail before and after C-rate test as shown in **Figure 5**. The semi-circle can be divided into two regions; the one in the high frequency region defines the charge transfer ($R_{ct}$) and at the medium frequency region resulted from the solid-electrolyte interface resistance ($R_{SEI}$) (**Figure 5a)**. The line showed the Warburg Impedance where the $Na^+$ ion diffusion can be calculated [54]. The Nyquist plot data was fit by using EC Lab Software with the respected equivalent circuit, hence the resistances were shown in **Table 2**. $R_{total}$ was the sum of the $R_{ct}$ and $R_{SEI}$, they became smaller after $30^{th}$ cycles due to the nickel sulfide particle size reduction and stable solid electrolyte interface formation [55]. $Na^+$ ion diffusion coefficient ($D_{Na+}$) was calculated from the Nyquist plot low frequency region which was represented as inclined line by using the following equation:

$$D_{Na^+}=R^2T^2/(2A^2n^4F^4C^2\sigma^2) \quad (1)$$

Where $D_{Na^+}$ is $Na^+$ ion diffusion rate ($cm^2 \cdot s^{-1}$), R is the gas constant (8.314 $J \cdot mol^{-1} \cdot K^{-1}$), T is the temperature (298 K), A is the electrode surface area (1.21 $cm^2$), n is the number of electrons per molecule during oxidation (n=1), F is the Faraday constant (96,500 $C \cdot mole^{-1}$), C is concentration of $Na^+$ ($10^{-3}$ $mol \cdot cm^{-3}$) in

the electrolyte and σ is the Warburg factor which was estimated by drawing the ($Z_{re}$) versus ($\omega^{-0.5}$) graph and calculated to the line slope as shown in **Figure 5b** [56, 57] via the following equation:

$$Z_{Re} = R_s + R_{ct} + \sigma\omega^{-0.5} \quad (2)$$

Diffusion coefficients were calculated to be $1.81 \times 10^{-16}$ and $3.5 \times 10^{-15}$ $cm^2 \cdot s^{-1}$ before and after 30 cycles C-rate test. The $Na^+$ ions diffusion rate increased upon cycling, in line with the decrease of the charge transfer resistance which was summarized in **Table 2**.

Moreover, the electrode surface was analyzed before and after C-rate tests and the resulting scanning electron microscopy image are presented in **Figure 5e** and **5f**, respectively. No surface cracks were observed during sodiation/desodiation process even though harsh cycling conditions were applied. The reason could be the choice of the binder. Na-alginate binder is used for the electrode preparations whose rich and homogenously distributed carboxylic and hydroxylic groups could provide self-healing properties during charge-discharge [58, 59]. However, at much longer cycles (after 500 cycles at 591 $mA \cdot g^{-1}$) some visible cracks were detected (Figure SI-3).

## 4. Conclusions

Herein, firstly Ni-MOF was synthesized from bio-available gallic acid in water. Then, a NiS/C composite was successfully prepared from a Ni containing MOF via one-step procedure in the presence of sulfur powder. After concurrent sulfuration and carbonization steps under thermal treatment, amorphous carbon encapsulated crystalline NiS nanoparticles were obtained that was characterized by X-ray power diffraction, scanning/transmission electron microscopy and X-Ray Photoelectron Spectroscopy. Carbon encapsulation not only assists conductivity increase but also prevents volume expansion of NiS during discharge. Later, NiS/C composite anode was tested as an anode material in the field of sodium ion batteries. Enhanced electrochemical performance at higher current densities without noticeable electrode surface cracks and pulverizations were noted. Thus, the MOF driven strategy could be considered beneficial to synthesize electro-active materials.

## Conflicts of interest

There are no conflicts to declare


## Acknowledgements

Ahmet Nazım is thanked for the SEM measurements and Adem Şen for the TGA and XRD measurements. The authors acknowledge Turkish Academy of Sciences, in the framework of the Young Scientist Award Program (TUBA-GEBIP/2018). This work is a part of doctorate thesis of Mehbare Dogrusoz.


## References


1. Hwang, J.-Y., S.-T. Myung, and Y.-K. Sun, *Sodium-ion batteries: present and future.* Chemical Society Reviews, 2017. **46**(12): p. 3529-3614.
2. Liang, Y., et al., *Nanocomposite materials for the sodium–ion battery: a review.* Small, 2018. **14**(5): p. 1702514.
3. Tarascon, J.-M., *Na-ion versus li-ion batteries: Complementarity rather than competitiveness.* Joule, 2020. **4**(8): p. 1616-1620.

4. Vaalma, C., et al., *A cost and resource analysis of sodium-ion batteries.* Nature Reviews Materials, 2018. **3**(4): p. 1-11.
5. Stevens, D. and J. Dahn, *High capacity anode materials for rechargeable sodium-ion batteries.* Journal of the Electrochemical Society, 2000. **147**(4): p. 1271.
6. Ponrouch, A., A. Goñi, and M.R. Palacin, *High capacity hard carbon anodes for sodium ion batteries in additive free electrolyte.* Electrochemistry communications, 2013. **27**: p. 85-88.
7. Zhang, W., et al., *Sodium-ion battery anodes: status and future trends.* EnergyChem, 2019. **1**(2): p. 100012.
8. Luo, M., et al., *Metal selenides for high performance sodium ion batteries.* Chemical Engineering Journal, 2020. **380**: p. 122557.
9. Sun, D., et al., *A layered Bi 2 Te 3 nanoplates/graphene composite with high gravimetric and volumetric performance for Na-ion storage.* Sustainable Energy & Fuels, 2019. **3**(11): p. 3163-3171.
10. Yu, X.Y. and X.W. Lou, *Mixed metal sulfides for electrochemical energy storage and conversion.* Advanced Energy Materials, 2018. **8**(3): p. 1701592.
11. Xiao, Y., S.H. Lee, and Y.K. Sun, *The application of metal sulfides in sodium ion batteries.* Advanced energy materials, 2017. **7**(3): p. 1601329.
12. Rui, X., H. Tan, and Q. Yan, *Nanostructured metal sulfides for energy storage.* Nanoscale, 2014. **6**(17): p. 9889-9924.
13. Kim, J.-S., et al., *The discharge properties of Na/Ni3S2 cell at ambient temperature.* Journal of Power Sources, 2008. **178**(2): p. 852-856.
14. Wang, J., et al., *Synthesis of NiS/carbon composites as anodes for high-performance sodium-ion batteries.* Journal of Solid State Electrochemistry, 2017. **21**(10): p. 3047-3055.
15. Bi, R., et al., *Metal–organic frameworks derived hollow NiS 2 spheres encased in graphene layers for enhanced sodium-ion storage.* Journal of Materials Chemistry A, 2018. **6**(29): p. 14077-14082.
16. Yu, S.H. and M. Yoshimura, *Fabrication of Powders and Thin Films of Various Nickel Sulfides by Soft Solution-Processing Routes.* Advanced Functional Materials, 2002. **12**(4): p. 277-285.
17. Zhao, X., et al., *Design of coherent anode materials with 0D Ni 3 S 2 nanoparticles self-assembled on 3D interconnected carbon networks for fast and reversible sodium storage.* Journal of Materials Chemistry A, 2017. **5**(16): p. 7394-7402.
18. Bruce, P.G., B. Scrosati, and J.M. Tarascon, *Nanomaterials for rechargeable lithium batteries.* Angewandte Chemie International Edition, 2008. **47**(16): p. 2930-2946.
19. Zhao, F., et al., *Stabilizing nickel sulfide nanoparticles with an ultrathin carbon layer for improved cycling performance in sodium ion batteries.* Nano Research, 2016. **9**(10): p. 3162-3170.
20. Zhang, D., et al., *Engineering Hierarchical Hollow Nickel Sulfide Spheres for High-Performance Sodium Storage.* Advanced Functional Materials, 2016. **26**(41): p. 7479-7485.
21. Maurin, G., et al., *The new age of MOFs and of their porous-related solids.* Chemical Society Reviews, 2017. **46**(11): p. 3104-3107.
22. Zhou, H.-C., J.R. Long, and O.M. Yaghi, *Introduction to metal–organic frameworks.* Chemical reviews, 2012. **112**(2): p. 673-674.
23. Chen, T., et al., *Recent progress on metal–organic framework-derived materials for sodium-ion battery anodes.* Inorganic Chemistry Frontiers, 2020. **7**(3): p. 567-582.
24. Liu, B., et al., *Metal-organic framework as a template for porous carbon synthesis.* Journal of the American Chemical Society, 2008. **130**(16): p. 5390-5391.

25. Li, Y., et al., *MOF-derived metal oxide composites for advanced electrochemical energy storage.* Small, 2018. **14**(25): p. 1704435.
26. Zou, G., et al., *Metal–organic framework-derived materials for sodium energy storage.* Small, 2018. **14**(3): p. 1702648.
27. Feller, R.K. and A.K. Cheetham, *Fe (III), Mn (II), Co (II), and Ni (II) 3, 4, 5-trihydroxybenzoate (gallate) dihydrates; a new family of hybrid framework materials.* Solid state sciences, 2006. **8**(9): p. 1121-1125.
28. Zhu, J., et al., *M-Gallate (M= Ni, Co) Metal–Organic Framework-Derived Ni/C and Bimetallic Ni–Co/C Catalysts for Lignin Conversion into Monophenols.* ACS Sustainable Chemistry & Engineering, 2019. **7**(15): p. 12955-12963.
29. Cooper, L., et al., *A biocompatible porous Mg-gallate metal–organic framework as an antioxidant carrier.* Chemical communications, 2015. **51**(27): p. 5848-5851.
30. Shirley, D.A., *High-resolution X-ray photoemission spectrum of the valence bands of gold.* Physical Review B, 1972. **5**(12): p. 4709.
31. Guan, B., et al., *Synthesis of hierarchical NiS microflowers for high performance asymmetric supercapacitor.* Chemical Engineering Journal, 2017. **308**: p. 1165-1173.
32. Bommier, C., et al., *Predicting capacity of hard carbon anodes in sodium-ion batteries using porosity measurements.* Carbon, 2014. **76**: p. 165-174.
33. Haridas, A.K., et al., *Simple design of an in situ generated iron sulfide/carbon heterostructure with N, S codoping for high performance lithium/sodium-ion batteries.* Applied Surface Science, 2021. **554**: p. 149587.
34. Yang, J., et al., *Electrochemical performances investigation of NiS/rGO composite as electrode material for supercapacitors.* Nano Energy, 2014. **5**: p. 74-81.
35. Wang, L., et al., *Engineering yolk–shell P-doped NiS 2/C spheres via a MOF-template for high-performance sodium-ion batteries.* Journal of Materials Chemistry A, 2020. **8**(17): p. 8612-8619.
36. Zhu, K., et al., *Metal-Organic Frameworks derived novel hierarchical durian-like nickel sulfide (NiS2) as an anode material for high-performance sodium-ion batteries.* Materials Letters, 2017. **197**: p. 180-183.
37. Nesbitt, H., D. Legrand, and G. Bancroft, *Interpretation of Ni2p XPS spectra of Ni conductors and Ni insulators.* Physics and Chemistry of Minerals, 2000. **27**(5): p. 357-366.
38. Xu, J., et al., *Facile synthesis of NiS anchored carbon nanofibers for high-performance supercapacitors.* Applied Surface Science, 2018. **434**: p. 112-119.
39. Fan, S., et al., *Construction of complex NiS multi-shelled hollow structures with enhanced sodium storage.* Energy Storage Materials, 2019. **23**: p. 17-24.
40. Rufael, T., et al., *Adsorption and reactions of benzenethiol on the Ni (111) surface.* The Journal of Physical Chemistry, 1994. **98**(49): p. 13022-13027.
41. Smart, R.S.C., W.M. Skinner, and A.R. Gerson, *XPS of sulphide mineral surfaces: metal-deficient, polysulphides, defects and elemental sulphur.* Surface and Interface Analysis: An International Journal devoted to the development and application of techniques for the analysis of surfaces, interfaces and thin films, 1999. **28**(1): p. 101-105.
42. Van der Heide, H., et al., *X-ray photoelectron spectra of 3d transition metal pyrites.* Journal of Solid State Chemistry, 1980. **33**(1): p. 17-25.
43. Chen, J., et al., *Sulfidation of NiMn-layered double hydroxides/graphene oxide composites toward supercapacitor electrodes with enhanced performance.* Advanced Energy Materials, 2016. **6**(5): p. 1501745.

44. Chen, X., X. Wang, and D. Fang, *A review on C1s XPS-spectra for some kinds of carbon materials.* Fullerenes, Nanotubes and Carbon Nanostructures, 2020. **28**(12): p. 1048-1058.
45. Qu, C., et al., *MOF-derived α-NiS nanorods on graphene as an electrode for high-energy-density supercapacitors.* Journal of Materials Chemistry A, 2018. **6**(9): p. 4003-4012.
46. Thommes, M., et al., *Physisorption of gases, with special reference to the evaluation of surface area and pore size distribution (IUPAC Technical Report).* Pure and applied chemistry, 2015. **87**(9-10): p. 1051-1069.
47. Pan, Q., et al., *Reduced graphene oxide-induced recrystallization of NiS nanorods to nanosheets and the improved Na-storage properties.* Inorganic chemistry, 2014. **53**(7): p. 3511-3518.
48. Liu, Y., et al., *MnFe2O4@ C nanofibers as high-performance anode for sodium-ion batteries.* Nano Letters, 2016. **16**(5): p. 3321-3328.
49. Park, G.D., J.S. Cho, and Y.C. Kang, *Sodium-ion storage properties of nickel sulfide hollow nanospheres/reduced graphene oxide composite powders prepared by a spray drying process and the nanoscale Kirkendall effect.* Nanoscale, 2015. **7**(40): p. 16781-16788.
50. Aydogdu, A., G. Sumnu, and S. Sahin, *Fabrication of gallic acid loaded hydroxypropyl methylcellulose nanofibers by electrospinning technique as active packaging material.* Carbohydrate polymers, 2019. **208**: p. 241-250.
51. Li, J., et al., *Design of pomegranate-like clusters with NiS 2 nanoparticles anchored on nitrogen-doped porous carbon for improved sodium ion storage performance.* Journal of Materials Chemistry A, 2018. **6**(15): p. 6595-6605.
52. Shuang, W., et al., *Nitrogen-doped carbon shell-confined Ni3S2 composite nanosheets derived from Ni-MOF for high performance sodium-ion battery anodes.* Nano Energy, 2019. **62**: p. 154-163.
53. Xu, S., et al., *Construction of NiS Nanosheets Anchored on the Inner Surface of Nitrogen-Doped Hollow Carbon Matrixes with Enhanced Sodium and Potassium Storage Performances.* ACS Applied Energy Materials.
54. Wang, G., Z. Liu, and P. Liu, *Co2SnO4–multiwalled carbon nanotubes composite as a highly reversible anode material for lithium-ion batteries.* Electrochimica acta, 2011. **56**(25): p. 9515-9519.
55. Li, T., et al., *Assembled NiS nanoneedles anode for Na-ion batteries: Enhanced the performance by organic hyperbranched polymer electrode additives.* Journal of Power Sources, 2020. **451**: p. 227796.
56. Cui, J., et al., *Enhanced conversion reaction kinetics in low crystallinity SnO 2/CNT anodes for Na-ion batteries.* Journal of Materials Chemistry A, 2016. **4**(28): p. 10964-10973.
57. Zhao, W., et al., *Carbon-coated CoP3 nanocomposites as anode materials for high-performance sodium-ion batteries.* Applied Surface Science, 2018. **445**: p. 167-174.
58. Bridel, J.-S., et al., *Key parameters governing the reversibility of Si/carbon/CMC electrodes for Li-ion batteries.* Chemistry of materials, 2010. **22**(3): p. 1229-1241.
59. Dogrusoz, M. and R. Demir-Cakan, *Mechanochemical synthesis of SnS anodes for sodium ion batteries.* International Journal of Energy Research, 2020. **44**(13): p. 10809-10820.

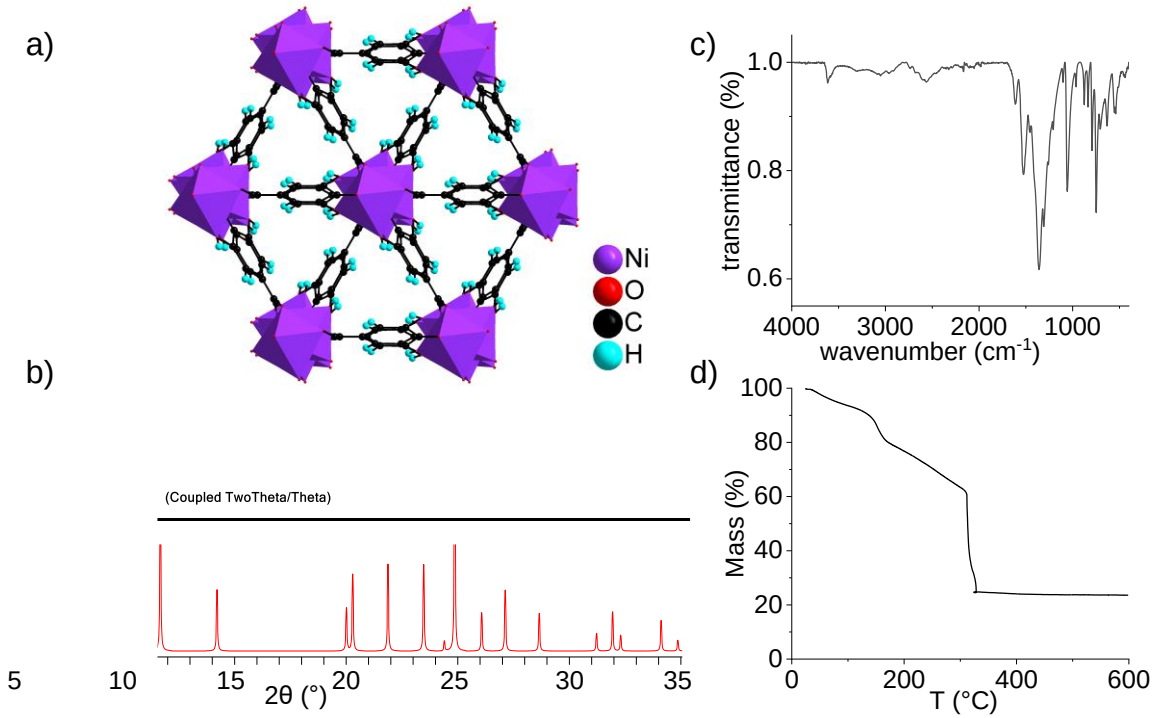


**Figure 1.** The Ni gallate MOF $Ni(C_7H_4O_5).2H_2O$. **a)** Crystal structure, **b)** experimental (black) and calculated (red) powder XRD patterns, **c)** infrared spectrum, **d)** thermogravimetric analysis.

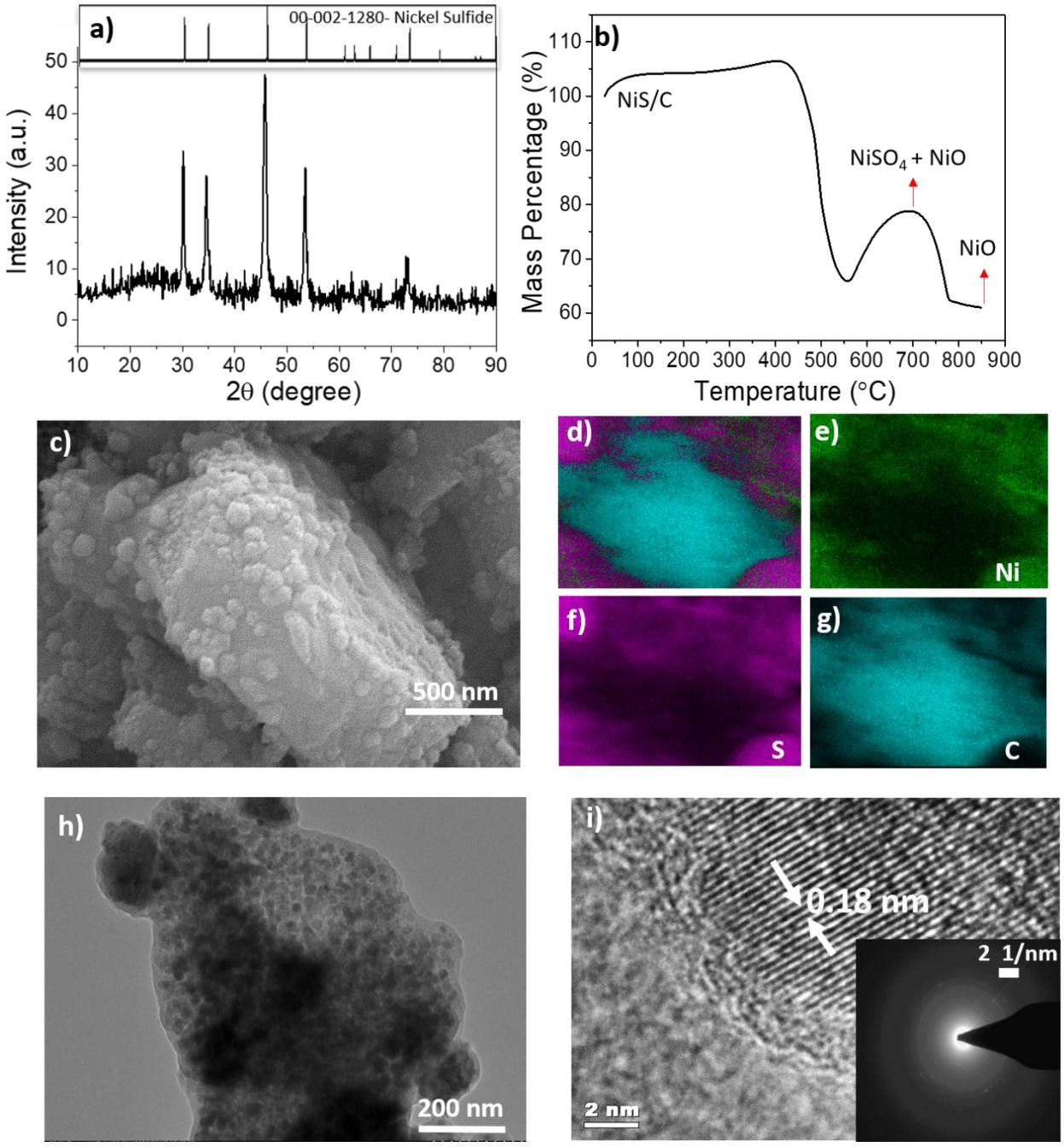


**Figure 2**. a) X-ray diffraction pattern of NiS/C, b) TGA curve of NiS/C composite. Tests were performed from the room temperature to 850 °C with 10 °C·min-1 rate under air atmosphere), c) SEM view of NiS/C, d-g) Overlay, Nickel, Sulfur and Carbon elemental mapping of the NiS/C powder, h) TEM image of NiS/C, i) HRTEM view of NiS/C.

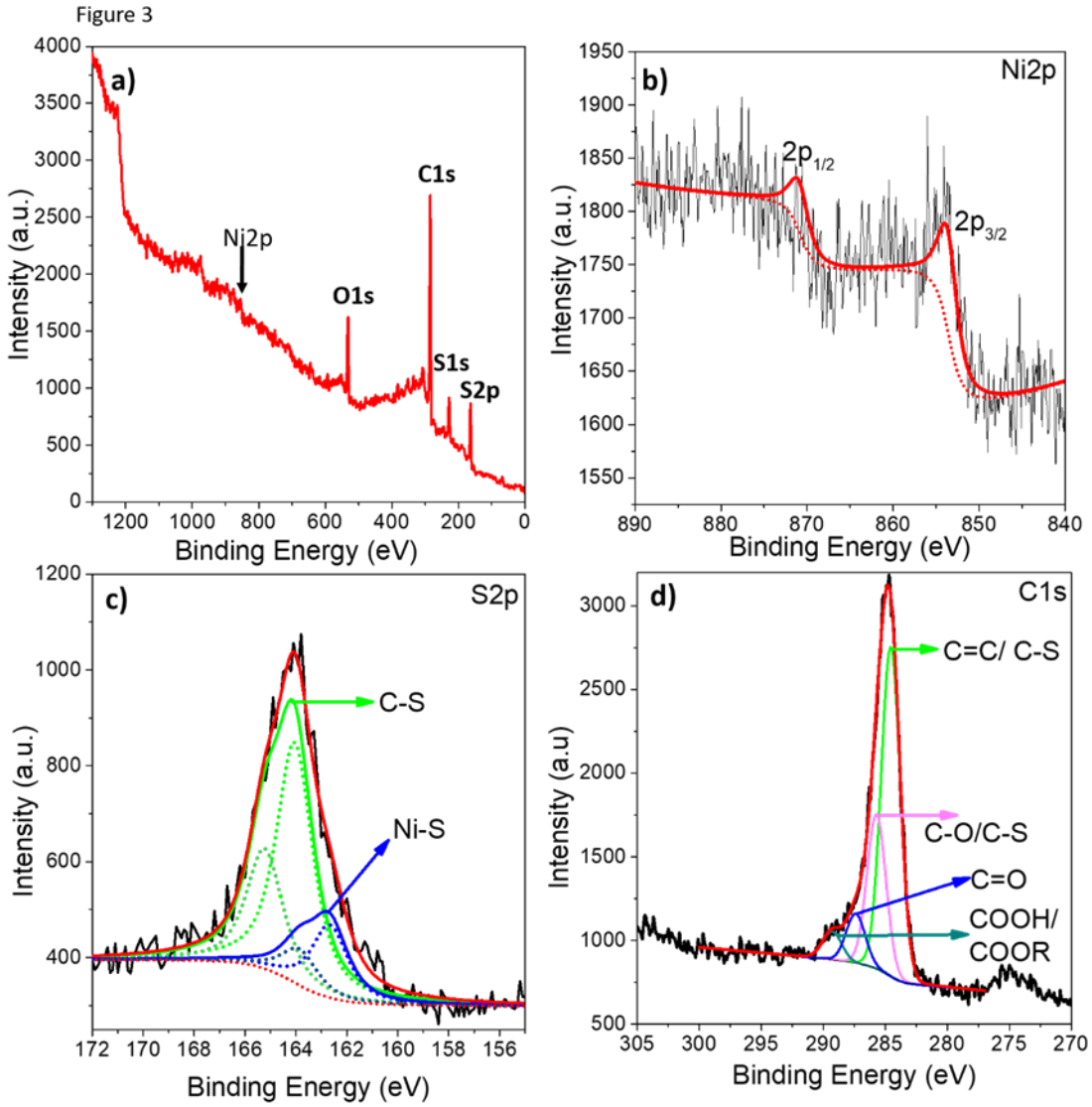


**Figure 3.** XPS spectra of a) Survey, b) Ni2p, c) S2p, d) C1s.

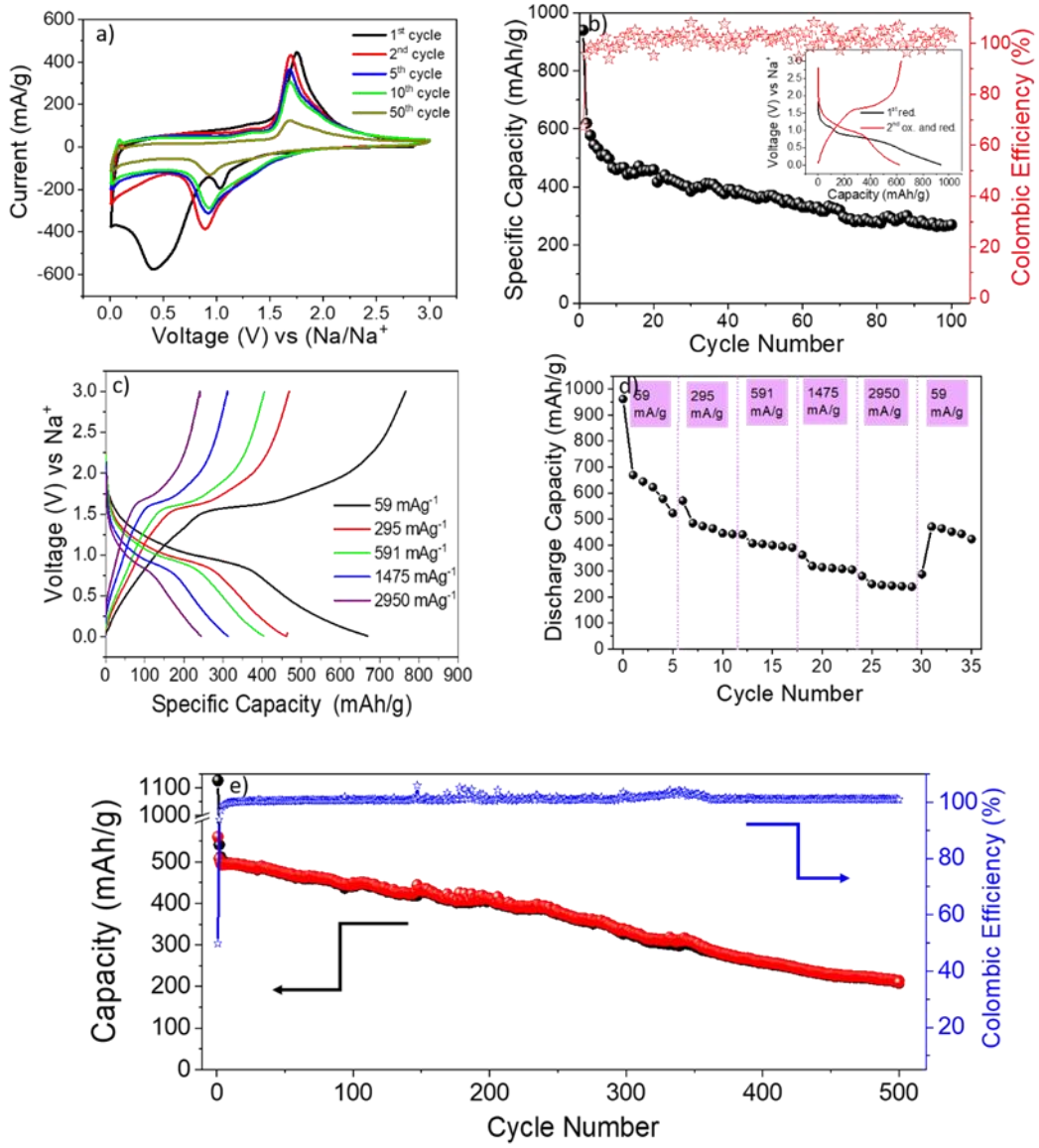


**Figure 4 a)** Cyclic voltommogram of NiS/C anode vs Na/ $Na^+$ at a scan rate of 0.1 $mV \cdot s^{-1}$, **b)** Galvanostatic charge /discharge test of NiS/C at 59 $mA \cdot g^{-1}$ current density, **b)** Charge –Discharge profile of NiS/C composite at different current rates, **d)** Rate capability test of NiS/C anode, e) Galvanostatic charge /discharge test of NiS/C at 591 $mA \cdot g^{-1}$. **Note:** Electrolyte is 1M $NaClO_4$ in PC 5 wt% FEC.

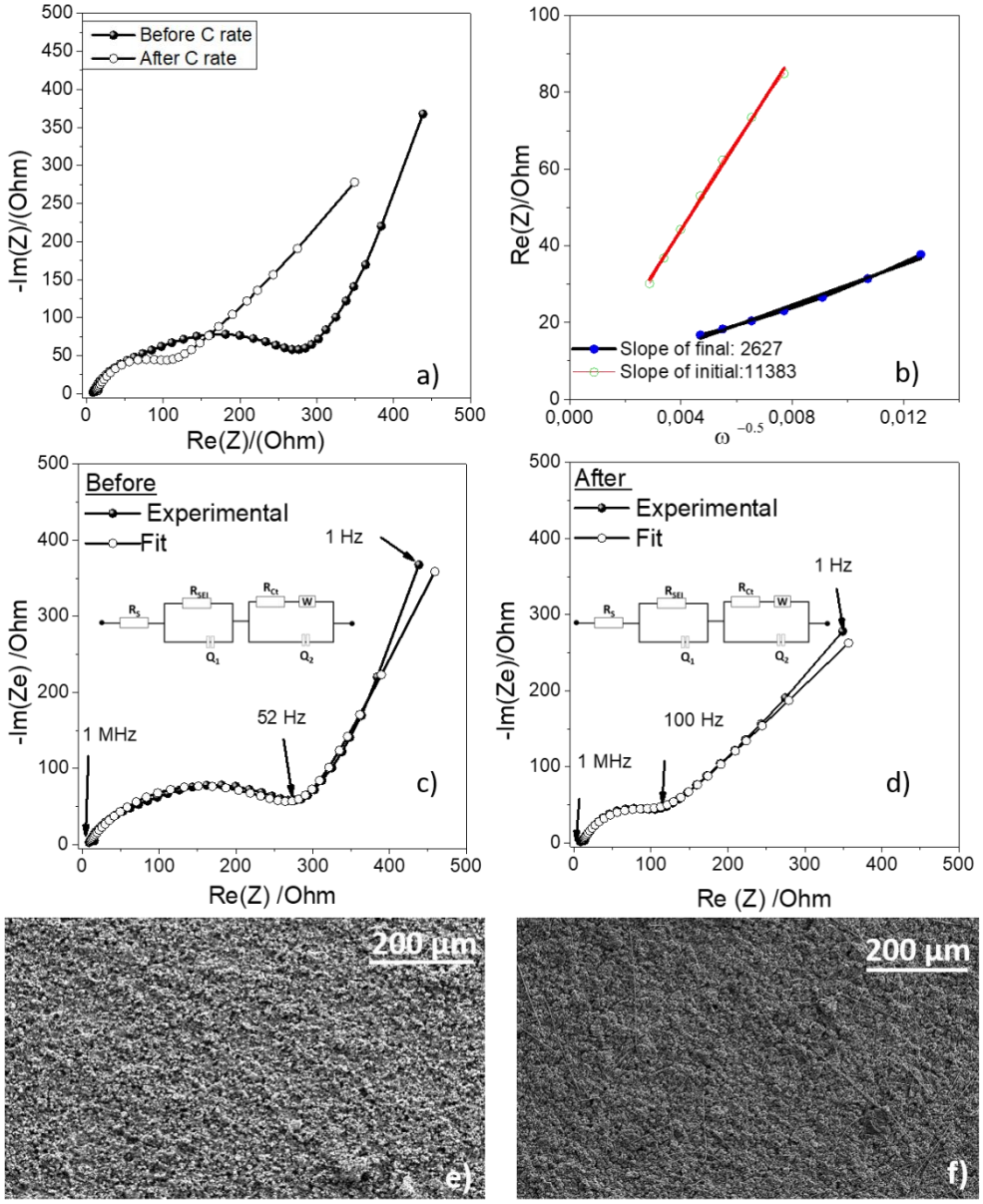


**Figure 5 a)** Impedance Spectra of NiS/C anode before and after C-rate cycling. **b)** Relationship of $Z_{Re}$ vs $\omega^{-0.5}$ in low frequency region. **c)** Impedance Spectra fit data before cycling, **d)** after cycling. **e-f)** Electrode surface Scanning Electron Microscopy view before and after cycling respectively.

**Table 1.** Comparison of the performances of MOF derived nickel sulfide carbon composite anodes for sodium ion batteries.

| Material | Organic Linker | $Ni_xS_y$ / C ratio | Electrolyte, Binder | Reversible Capacity and Current rate | Sulfuration Temperature and Atmosphere | Ref. |
|---|---|---|---|---|---|---|
| **NiS/ N-CNT** | PVP | 46 % / 54% | 1M $NaPF_6$ in EC:DEC 2% FEC, PVdF | 300 $mAh{\cdot}g^{-1}$ @100 $mA{\cdot}g^{-1}$ (800 cycles) | 500 °C, Argon | [39] |
| **$NiS_2$/C** | 2-Methylimidazole | 68.8% / 31.2% | 1M $NaClO_4$ in EC:DEC 1% FEC, CMC | 186.9 $mAh{\cdot}g^{-1}$ @500 $mA{\cdot}g^{-1}$ (100 cycles) | 600 °C, Nitrogen | [36] |
| **$NiS_2$/NC** | | 74.3% / 25.7% | 1M $NaClO_4$ in EC:PC 5% FEC, CMC | 356.2 $mAh{\cdot}g^{-1}$ @500 $mA{\cdot}g^{-1}$ (300 cycles) | 350°C, Nitrogen | [51] |
| **$Ni_3S_2$** | 1,4-terephthalic acid | N/A | 1M $NaClO_4$ in EC:DEC 5% FEC, PVdF | 432.8 $mAh{\cdot}g^{-1}$ @200 $mA{\cdot}g^{-1}$ (100 cycles) | 600 °C, Argon | [52] |
| **$NiS_2$/P-C** | Trimesic acid | 88.7% / 11.3% | 1M $NaClO_4$ in EC:DMC 5% FEC, PVdF | 766.8 $mAh{\cdot}g^{-1}$ @500 $mA{\cdot}g^{-1}$ (400 cycles) | 350 °C, Argon | [35] |
| **h-NiS/C-N** | 2-Methylimidazole | 71.4% / 28.6% | 1M $NaClO_4$ in EC:DEC 5% FEC, PVdF | 290 $mAh{\cdot}g^{-1}$ @1000 $mA{\cdot}g^{-1}$ (1000 cycles) | 600 °C, Nitrogen | [53] |
| **NiS/C** | Gallic Acid | 72% / 28% | 1M $NaClO_4$ in PC 5% FEC, Na-alginate | 211 $mAh{\cdot}g^{-1}$ @591 $mA{\cdot}g^{-1}$ (500 cycles) | 600 °C, Nitrogen | Present Study |

**Table 2.** The estimated resistances of NiS/C anode before and after 30 cycles.

| States | $R_{ct}$ (Ω) | $R_{SEI}$ (Ω) | $R_{Total}$ (Ω) |
|---|---|---|---|
| **Fresh** | 278 | 174 | 452 |
| **After 30 cycles** | 80 | 11 | 91 |